Perovskite Solar Cells | Hot Paper

DOI: 10.1002/ange.201405334

A Fast Deposition-Crystallization Procedure for Highly Efficient Lead Iodide Perovskite Thin-Film Solar Cells**

Manda Xiao, Fuzhi Huang, Wenchao Huang, Yasmina Dkhissi, Ye Zhu, Joanne Etheridge, Angus Gray-Weale, Udo Bach, Yi-Bing Cheng, and Leone Spiccia**

Abstract: *Thin-film photovoltaics based on alkylammonium lead iodide perovskite light absorbers have recently emerged as a promising low-cost solar energy harvesting technology. To date, the perovskite layer in these efficient solar cells has generally been fabricated by either vapor deposition or a two-step sequential deposition process. We report that flat, uniform thin films of this material can be deposited by a one-step, solvent-induced, fast crystallization method involving spin-coating of a DMF solution of $CH_3NH_3PbI_3$ followed immediately by exposure to chlorobenzene to induce crystallization. Analysis of the devices and films revealed that the perovskite films consist of large crystalline grains with sizes up to microns. Planar heterojunction solar cells constructed with these solution-processed thin films yielded an average power conversion efficiency of 13.9 ± 0.7 % and a steady state efficiency of 13 % under standard AM 1.5 conditions.*

Thin-film solar cells, such as dye-sensitized solar cells,[1] organic photovoltaics,[2] and colloidal nanocrystal solar cells,[3] can be assembled with low-cost materials and manufactured with cost-effective methods, and are considered very promising renewable energy technologies. Recently, alkylammonium lead(II) halides, such as $CH_3NH_3PbI_3$ and $CH_3NH_3PbI_xCl_{3-x}$ have been shown to be efficient photovoltaic materials with excellent light harvesting, high carrier mobility, and facile solution processability.[4–31] These organic–inorganic lead(II) complexes crystallize in the well-known perovskite structure with general formula ABX_3. Perovskite solar cells utilizing a mesoporous scaffold, such as titania or alumina, the lead iodide light absorber, and an organic hole transport material (HTM), typically spiro-OMeTAD (2,2′,7,7′-tetrakis-(*N*,*N*-di-p-methoxyphenylamine)-9,9′-bifluorene) have achieved a power conversion efficiency (PCE) of >10 %.[6,7] The PCEs were improved to 15 % by using a two-step sequential deposition technique, involving spin-coating of a PbI_2 followed by exposure to a solution of CH_3NH_3I to form $CH_3NH_3PbI_3$, or a dual-source vapor-deposition technique to fabricate a planar heterojunction solar cell.[16–18]

Compared to the mesostructured perovskite solar cells, in which the light absorber is typically deposited on a 300 nm mesoporous scaffold, planar devices lacking this scaffold, have attracted interest because of their simpler structure.[17,18] To avoid the shunting in such planar devices, a nonporous homogenous perovskite film must be deposited. However, films produced by the conventional spin-coating methods were found to be composed of large $CH_3NH_3PbI_3$ grains and many uncovered pin-hole areas.[16] This structure arose from slow crystallization owing to the high boiling point of DMF (*N*,*N*-dimethylformamide, 153 °C), and crystal growth arising from a slow nucleation rate during natural drying process in spin-coating. To date, the $CH_3NH_3PbI_3$ layer in the most efficient planar solar cells has been fabricated by either vapor deposition, a two-step sequential solution deposition, or a vapor-assisted two-step reaction process.[16,17,20] The vapor-deposition process is likely to increase the manufacturing cost whereas the sequential two-step deposition procedure will involve longer overall processing time.[16] Therefore, a faster, facile solution-processing technique that can regulate the perovskite crystallization process and produce high-quality films with controlled morphology is highly desirable for the construction of planar devices with superior performances.

[*] M. D. Xiao, Prof. Dr. L. Spiccia
School of Chemistry, Monash University
Victoria 3800 (Australia)
E-mail: leone.spiccia@monash.edu

Dr. F. Z. Huang, W. C. Huang, Y. Dkhissi, Dr. Y. Zhu, Prof. Dr. J. Etheridge, Prof. Dr. U. Bach, Prof. Dr. Y.-B. Cheng
Department of Materials Engineering, Monash University
Victoria 3800 (Australia)
E-mail: yibing.cheng@monash.edu

Prof. Dr. J. Etheridge
Monash Centre for Electron Microscopy, Monash University
Victoria 3800 (Australia)

Prof. Dr. U. Bach
Melbourne Centre for Nanofabrication
151 Wellington Road, Clayton, Victoria 3168 (Australia)
and
CSIRO, Materials Science and Engineering
Clayton South, Victoria 3169 (Australia)

Dr. A. Gray-Weale
Department of Chemistry, University of Melbourne
Victoria 3010 (Australia)

[**] We thank Mr. D. Vowles and Dr. Y. Chen for assistance with preparation of the FIB sample, and Dr. T. Williams for maintenance of the TEM imaging lens series. We acknowledge the Australian Research Council for providing equipment and fellowship support, the Australian Renewable Energy Agency, the Australian Centre for Advanced Photovoltaics, Victorian State Government (DBI-VSA and DPI-ETIS) for financial support as well as Monash University Centre for Electron Microscopy and the Advanced Microscopy Facility at The University of Melbourne for electron microscopy access. U.B. thanks the CSIRO for providing support through an OCE Science Leader position. Y.Z. was supported by the ARC grant (DP110104734) and the Tecnai F20 TEM and Quanta 3D FIB/FEG-SEM were funded by ARC grants LE110100223 and LE0882821, respectively.

Supporting information for this article is available on the WWW under http://dx.doi.org/10.1002/anie.201405334.

Attempts have been made to control the crystallization of $CH_3NH_3PbI_3$ during solution-processing by partially substituting I^- with Cl^- to create lattice distortions or introducing additives, such as 1,8-diiodooctane, to enhance the crystallization.[14,32] Although good PCEs of approximately 12% were achieved, they were limited by quality of the perovskite films.

Herein, we report a one-step, solvent-induced, fast crystallization-deposition (FDC) method that results in flat, highly uniform $CH_3NH_3PbI_3$ thin films. This simple approach involves the spin-coating of a DMF solution of $CH_3NH_3PbI_3$ on a substrate, followed immediately by exposure of the wet film to a second solvent, such as chlorobenzene (CBZ), to induce crystallization. This FDC spin-coating method offers the advantage of single-step processing and short depositions time as the film formation is complete within 1 min. Perovskite films consisting of highly crystalline single grains are produced which when used to construct planar heterojunction solar cells yielded a maximum PCE of 16.2% under standard AM 1.5 conditions. Moreover, the process is highly reproducible with average efficiencies of 13.9 ± 0.7% for 10 devices prepared in one batch. We believe that this facile method can be applied for the fast production of highly efficient $CH_3NH_3PbI_3$ based solar cells.

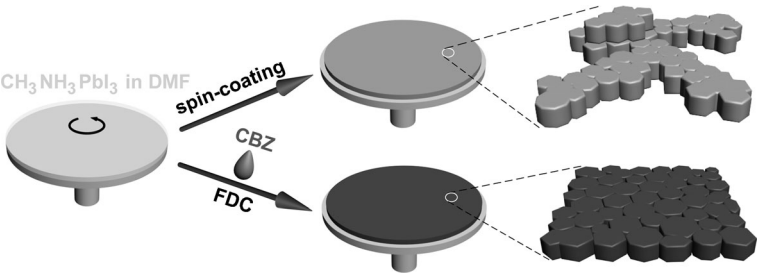

Figure 1. Schematic illustration of the FDC process and conventional spin-coating process for fabricating perovskite films. Conventional spin-coating (top) results in a shiny gray film composed of non-uniform large crystals as a result of slow crystallization. In the FDC process (bottom), a second solvent (e.g. chlorobenzene) introduced on top of the wet film during the spin-coating process induces fast crystallization of uniformly sized perovskite grains.

The FDC method for preparing the $CH_3NH_3PbI_3$ films is shown in Figure 1. First, a dense TiO_2 layer (ca. 30 nm thick) was deposited on a fluorine-doped tin oxide (FTO) coated glass using spray pyrolysis. A DMF solution of $CH_3NH_3PbI_3$ (45 wt%) was then spin-coated on the TiO_2 layer at 5000 rpm. After a specific delay time (e.g., 6 s), a second solvent was quickly added to the substrate. The role of the second solvent is to rapidly reduce the solubility of $CH_3NH_3PbI_3$ in the mixed solvent and thereby promoting fast nucleation and growth of the crystals in the film. A series of 12 solvents was tested, including chlorobenzene, benzene, xylene, toluene, methanol, ethanol, ethylene glycol, 2-propanol, chloroform, THF, acetonitrile, and benzonitrile. An instant darkening of the film when the second solvent was added was taken as evidence of the formation of the desired material. In contrast, during a conventional spin-coating process where no second solvent was added, the wet film dried slowly and a shiny-gray film was obtained. The films were then subjected to annealing at 100°C for 10 min to evaporate any residual solvent and to further promote crystallization.

Analysis of these films by scanning electron microscopy (SEM) revealed strikingly different morphologies. The films produced by the FDC technique with the addition of chlorobenzene, benzene, xylene, toluene, 2-propanol, and chloroform, in which $CH_3NH_3PbI_3$ has low solubility, exhibit full surface coverage and are composed of micron-sized grains (Figure 2a,b, and Supporting Information Figure S1a–e). The central area in the films was non-uniform when 2-propanol or chloroform was introduced (images not shown) while the grain morphology in the films obtained with the addition of chlorobenzene, benzene, xylene and toluene are uniform over the entire substrate. We used chlorobenzene as a representative solvent in further studies. The transmission electron microscopy (TEM) image of the $CH_3NH_3PbI_3$ film prepared with chlorobenzene addition reveals clear lattice fringes (Figure 2c) indicating the formation of a crystalline structure with a lattice spacing of (0.31 ± 0.01) nm, which could be indexed as (004) or (220) of the tetragonal $CH_3NH_3PbI_3$ phase. This was further confirmed by the X-ray diffraction (XRD) patterns (Figure 2f). Intense diffraction peaks at 14.08°, 23.48°, 28.40°, and 31.86° can be respectively assigned to (110), (211), (220), and (310)

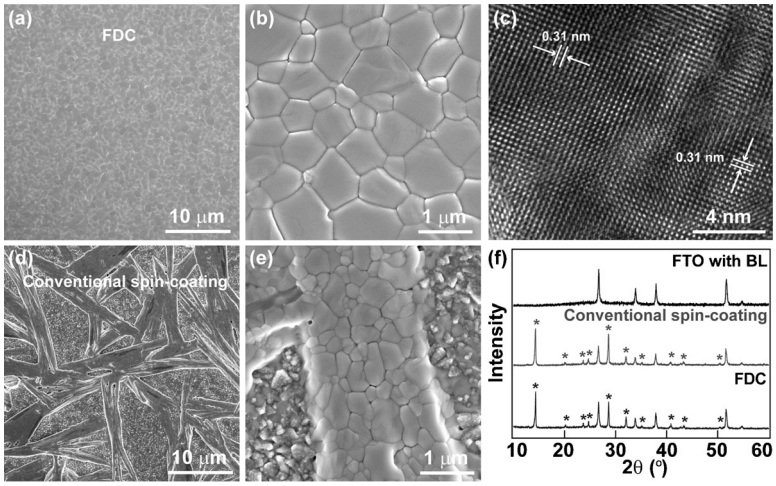

Figure 2. Morphological and structural characterization of $CH_3NH_3PbI_3$ films prepared by FDC and a conventional spin-coating process. The concentration of the perovskite solution was 45 wt%. a,b) Low- and high-magnification SEM images of the surface of a $CH_3NH_3PbI_3$ film prepared by FDC with the addition of chlorobenzene. c) An atomic resolution TEM image of a $CH_3NH_3PbI_3$ grain from a film produced by FDC, showing a pseudo-cubic lattice. d,e) Low- and high-magnification SEM images of a film prepared by conventional spin-coating. f) XRD patterns of the films corresponding to (a) and (d). The XRD pattern of the TiO_2 blocking layer (BL) coated FTO substrate is shown for comparison. The XRD peak intensity has been normalized. The peaks assigned to $CH_3NH_3PbI_3$ crystals are marked with asterisks.

diffractions of the tetragonal $CH_3NH_3PbI_3$ phase.[16,33] For solvents in which CH_3NH_3I has high solubility, for example, methanol, ethanol, and ethylene glycol, a yellow film with large PbI_2 crystals was obtained instead of $CH_3NH_3PbI_3$ (Figure S1 f–h). Other solvents, including THF, acetonitrile, and benzonitrile, in which of $CH_3NH_3PbI_3$ is moderately soluble, produced an almost transparent film (Figure S1 i). In contrast to the film obtained by FDC, the shiny-gray film obtained by conventional spin-coating contains larger rod-like grains with an incomplete coverage on the substrate (Figure 2 d), which is in accordance with previous observations.[15,16] A closer examination of these large rod grains reveals that the grain structure is similar to that of $CH_3NH_3PbI_3$ obtained by FDC (Figure 2 e). This is further confirmed by the XRD patterns obtained for both films (Figure 2 f). An advantage of the FDC method is that the thickness of the perovskite film can be easily controlled by changing the concentration of the perovskite solution, thus, films with a thickness of 150, 260, 350, and 550 nm were prepared from DMF solutions containing 25, 35, 45, and 55 wt % of $CH_3NH_3PbI_3$, respectively. Larger grain sizes were also found for the thicker films (Figure S2). The UV/Vis spectra indicate that, in the 350–700 nm region, 80–90 % of the light passing through the FTO glass was absorbed by a 350 nm film and over 90 % absorption for a 550 nm thick film (Figure S3). Most significantly, the morphology of the FDC processed $CH_3NH_3PbI_3$ thin films is remarkably different from the majority of film microstructures produced by solution-based approaches.[15,16,18] Flat polygonal grains with triple junction grain boundaries are a predominant microstructural feature in our films, suggesting close packing of perovskite grains of a similar size along the film thickness direction. This characteristic may lead to improved charge transport properties for photovoltaic devices.

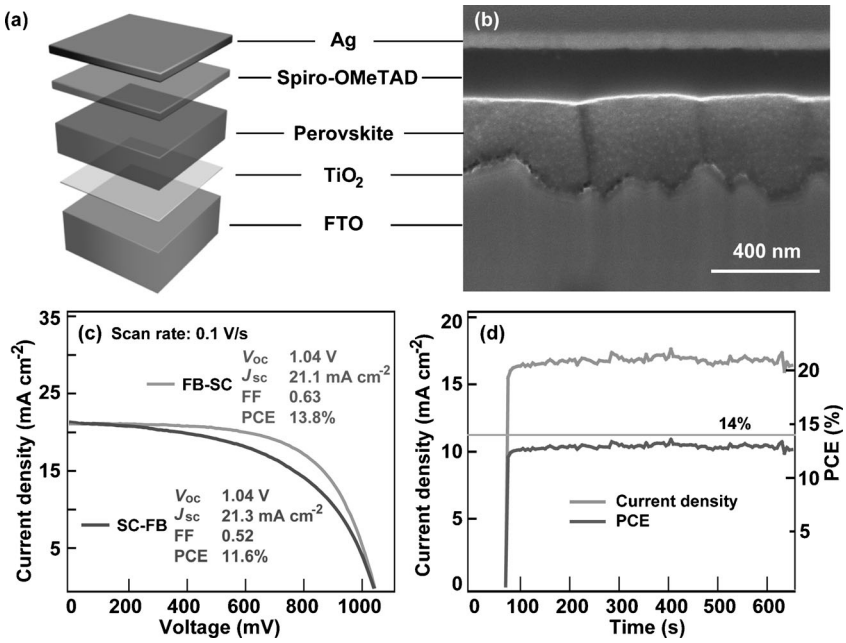

Figure 3. Device structure and photovoltaic characterization. a) Schematic illustration of a typical photovoltaic device. b) Cross-sectional SEM image of an optimized device. c) FB-SC and SC-FB *J--V* curves measured under AM 1.5 simulated sun light with a scan rate of 0.1 $V s^{-1}$ for a device prepared by FDC method using a 45 wt % perovskite solution. Inset are the detailed performance parameters for both scanning directions. d) Photocurrent density and PCE as a function of time for the same cell held at a forward bias of 0.77 V. The cell was placed in the dark prior to the start of the measurement.

To further probe the film formation process using FDC, we investigated the addition of the chlorobenzene solution onto the spinning wet films to initiate nucleation and crystal growth after different delay times from the start of spinning, 2, 4, or 8 s. Figure S4 shows the morphologies of the obtained $CH_3NH_3PbI_3$ films. To understand these observations, we can divide the spin-coating process into three stages.[34,35] In the first three seconds after spinning was commenced (stage 1), removal of excess precursor solution is a dominant process.[34] Introduction of chlorobenzene at this stage did not lead to full surface coverage possibly because the perovskite solution was far from supersaturation (Figure S4 a,d). In stage 2 (4–6 s), evaporation of the residue solvent occurs significantly concentrating the perovskite solution from which a dense and uniform film was formed when the second solvent was introduced (Figure S4 b,e). In stage 3 (after 7 s), the liquid film started to dry and heterogeneous crystallization occurs. Addition of chlorobenzene at this stage did not help to achieve a homogeneous perovskite film (Figure S4 c,f).

Solar cells were constructed with the perovskite films produced by the optimized FDC method. Figure 3 a,b illustrate the planar device structure and a cross-sectional SEM image, fabricated by focused ion beam (FIB) milling. Although gallium ion beam etching induced slight shrinkage of the spiro-OMeTAD layer at the cross-section, which is responsible for electron charging and a bright contrast at the edge of the $CH_3NH_3PbI_3$ layer, the optimized device can be seen to be clearly composed of a 30 nm thick dense TiO_2 layer on FTO, a 350 nm perovskite layer, a 180 nm spiro-OMeTAD layer, and a 70 nm thermally evaporated Ag layer as the back contact. Solar cells were also fabricated using FDC prepared $CH_3NH_3PbI_3$ films of different thickness and the films prepared by the conventional spin-coating techniques. The average photovoltaic parameters (Table 1) of these cells were measured under simulated AM 1.5 G illumination at an intensity of 100 mW cm^{-2}.

Solar cells utilizing the films prepared by conventional spin-coating exhibited a poor PCE of only 1.5 %, mainly because of cell shunting and poor light absorption arising from incomplete surface coverage.[36] In contrast, solar cells utilizing a 150 nm perovskite layer, produced by FDC, yielded a higher J_{sc} of 17 mA cm^{-2} and a much better PCE of 8 %, revealing the importance of full coverage of the perovskite film on the substrate. Increasing the film thickness from 150 nm to 350 nm led to higher J_{sc} and PCEs, which is mainly

Table 1: Device parameters for solar cells using perovskite films with different thicknesses prepared by conventional spin-coating and FDC.[a]

Cell	V_{oc} [V]	J_{sc} [mA cm^{-2}]	*FF*	PCE [%]
Conventional	0.52 ± 0.05	5.6 ± 0.9	0.52 ± 0.04	1.5 ± 0.3
FDC, 150 nm	0.77 ± 0.08	17.0 ± 0.2	0.61 ± 0.01	8.0 ± 0.1
FDC, 260 nm	0.96 ± 0.13	19.3 ± 0.3	0.63 ± 0.01	11.7 ± 0.3
FDC, 350 nm	0.98 ± 0.01	21.0 ± 0.9	0.68 ± 0.03	13.9 ± 0.7
FDC, 550 nm	0.97 ± 0.22	20.3 ± 0.2	0.60 ± 0.02	11.7 ± 0.2

[a] data for "FDC, 350 nm" is averaged from 10 devices and 4 devices for others.

attributed to the enhanced light absorption (Figure S2). A further increase in film thickness to 550 nm resulted in lower J_{sc} and V_{oc}, possibly a result of increased charge recombination. The reproducibility of the results was tested by fabricating a batch of 10 devices with an optimized film thickness of 350 nm (Table S1). The average PCE of 13.9 ± 0.7 %, is higher than that achieved in previous studies using the two-step sequential deposition and vacuum-based vapor deposition methods.[16,17] The high reproducibility is attributed to the high homogeneity of the $CH_3NH_3PbI_3$ film achieved by the FDC technique. Recently an anomalous hysteresis in the *J*--*V* curves of perovskite solar cells has been observed.[37,38] We therefore recorded the *J*--*V* curves of a typical solar cell prepared by the FDC method with different scanning directions (Figure 3c). A PCE of 13.8 % was recorded when using the conventional scan direction from forward bias (FB) to short circuit (SC) with a scan rate of 0.1 V s^{-1} while the opposite scan direction yielded an efficiency of 11.6 %. We also recorded the photocurrent of this cell held at a forward bias of 0.77 V as a function of time to gain some understanding of the stabilized power output under working conditions (Figure 3d). The photocurrent stabilizes within seconds to approximately 17 mA cm^{-2}, yielding a stabilized power conversion efficiency of 13.0 %, measured after 600 s. This indicates that FB to SC scans provide a more accurate representation of the cell's photovoltaic performance while still resulting in a relative overestimation of the steady state power output by about 5.8 %. The *J*–*V* curves were also recorded with scan rates ranging from 0.1 V s^{-1} to 0.01 V s^{-1} (Figure S5), revealing a weak scan-rate dependence of the hysteresis effect. In addition, for one cell measured under a light intensity of 100 mW cm^{-2} with a scanning direction from FB to SC and a scan rate of 0.1 V s^{-1}, the J_{sc}, V_{oc}, and fill factor are 21.1 mA cm^{-2}, 1.04 V, and 0.74, respectively, yielding a PCE of 16.2 % (Figure S6a). The incident photon-to-electron conversion efficiency (IPCE) of the device, shown in Figure S6b, exhibits a photocurrent onset at 800 nm and rises steeply to 76 % at 760 nm, in agreement with the band gap of $CH_3NH_3PbI_3$ and previous studies.[15–19] IPCEs above 80 % can be observed across a broad spectral region from 400–700 nm, and especially in the 400–600 nm range. Integration of the IPCE spectrum with the AM1.5G photon flux yields a current density of 21.5 mA cm^{-2}, which is in excellent agreement with the measured photocurrent density of 21.1 mA cm^{-2}. Further improvements in J_{sc} would be anticipated if the light absorption in the NIR region could be enhanced by utilizing, for example, plasmonic technologies.[39]

To investigate in detail the microstructure of the $CH_3NH_3PbI_3$ film produced by FDC, the cross-section of the grain structures was further characterized by TEM. Special care was taken to minimize the sample damage during cross-section fabrication by FIB milling. However, as shown in the bright-field TEM image (Figure S7), some milling damage is evident in the perovskite layer. Nevertheless, the macroscopic geometry of the film is retained and reveals, as expected, a 350 nm-thick $CH_3NH_3PbI_3$ layer on a dense TiO_2 layer, which shows a granular structure with grain sizes comparable to the layer thickness. No horizontal grain boundary is observed, suggesting that most perovskite grains span the thickness of the film. Grains without obvious FIB damage were selected and examined in more detail using selected-area-diffraction (SAD) and high resolution TEM. The perovskite was sensitive to electron beam irradiation unless care was taken to minimize the dose. Figure 4 shows the atomic resolution images from the top and bottom region of an individual perovskite grain, along with a SAD pattern from a much larger region in the center of the same grain. The lattice fringes in the two images have the same orientation (Figure 4b,d). In addition, the Fourier transform of these images and the SAD pattern all show the same strong perovskite diffraction spots aligned with the same orientation (Figure 4c,e), consistent with the whole perovskite grain

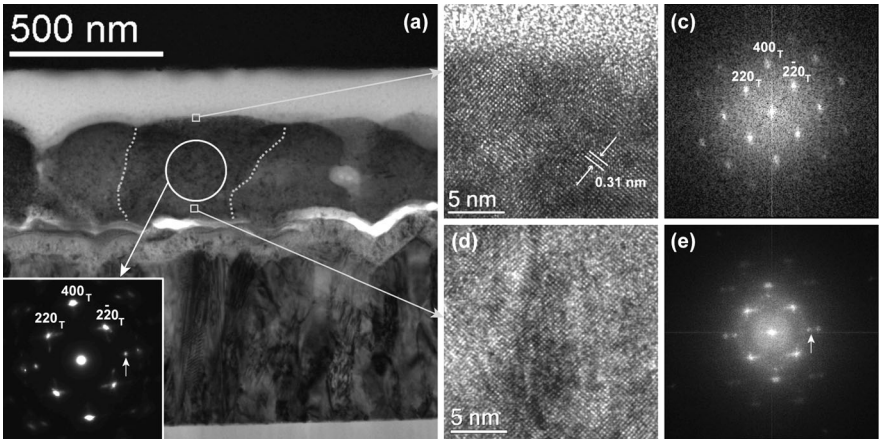

Figure 4. Characterization of the $CH_3NH_3PbI_3$ perovskite grain structures. a) TEM cross-sectional image of the FTO/TiO_2/$CH_3NH_3PbI_3$/Spiro-OMeTAD/Ag solar cell. Inset: SAD pattern taken from the region indicated by the circle. The boundaries of the selected grain are highlighted with dotted lines. b,d) Atomic resolution TEM images of the top and bottom region of an individual perovskite grain. c,e) Fourier transforms of (b) and (d), respectively. The major perovskite diffraction spots are indexed in white with a subscript T (tetragonal). The weaker diffraction spots indicated by arrows can be indexed as 130 from the tetragonal perovskite phase, but may also originate from a second phase.

being a single crystal. However, other weak reflections are also evident in these diffraction patterns. This may be due to localized loss of CH_3NH_3I under ion (and possibly electron) beam irradiation, leaving small regions of PbI_2, possibly on the surface. Because the (220) and (004) lattice spacings in the tetragonal perovskite phase are very similar to each other (both ca. 0.31 nm) and cannot be distinguished by our SAD or TEM study. Therefore, all the diffraction spots that are indexed as 220_T could also be indexed as 004_T. The single perovskite grains are believed to facilitate charge transport between electrodes because of the reduced number of defect and trap states at grain boundaries.[40] In addition, almost all the grains examined had no grain boundaries parallel to the plane of the two electrodes, which can lead to reduced electron scattering during charge transport. Both effects can contribute to efficient charge extraction. SAD patterns were also taken from 16 individual perovskite grains along the length of the perovskite layer (Figure S7). The specimen area illuminated by the electron beam in each case is a circle with a diameter of approximately 200 nm. As with the grain in Figure 4, most grains show strong primary diffraction spots associated with a single crystal of the tetragonal perovskite phase together with a number of weak diffraction spots, the majority of which are consistent with the FIB-induced PbI_2 phase. It is also evident that adjacent perovskite grains do not appear to share a common crystallographic axis.

In conclusion, a fast, single-step, solution-based deposition-crystallization method has been developed, which allows control over the dynamics of nucleation and grain growth of $CH_3NH_3PbI_3$, and achieves the rapid and reproducible fabrication of high-quality perovskite thin films. SEM analysis indicated that the perovskite thin films of controllable thickness can be prepared with large grain structures that fully cover the substrate. The application of these films in solar-cell construction led to an average PCE of $13.9 \pm 0.7\,\%$ and a steady state efficiency of 13 %. TEM analysis revealed that the perovskite film consisted of large crystalline grains which are free of grain boundaries parallel to the plane of the electrodes. The simplicity and the low-temperature solution processing characteristic of the FDC protocol is fully compatible with the construction of tandem devices using existing photovoltaic technologies, such as silicon-based solar cells and polymer solar cells.[41] We believe that this thin-film processing technology will not only benefit the perovskite-based photovoltaic devices but also bring new possibilities to perovskite-based hybrid optoelectronic devices, such as field effect transistors and light emitting diodes.

Received: May 16, 2014
Revised: June 18, 2014
Published online: July 22, 2014

Keywords: crystallization · light harvesting · perovskite solar cells · photovoltaics · thin films

[1] A. Yella, H.-W. Lee, H. N. Tsao, C. Y. Yi, A. K. Chandiran, M. K. Nazeeruddin, E. W.-G. Diau, C.-Y. Yeh, S. M. Zakeeruddin, M. Grätzel, *Science* **2011**, *334*, 629.
[2] G. Li, R. Zhu, Y. Yang, *Nat. Photonics* **2012**, *6*, 153.
[3] A. K. Rath, M. Bernechea, L. Martinez, F. P. G. de Arquer, J. Osmond, G. Konstantatos, *Nat. Photonics* **2012**, *6*, 529.
[4] A. Kojima, K. Teshima, Y. Shirai, T. Miyasaka, *J. Am. Chem. Soc.* **2009**, *131*, 6050.
[5] I. Chung, B. Lee, J. Q. He, R. P. H. Chang, M. G. Kanatzidis, *Nature* **2012**, *485*, 486.
[6] M. M. Lee, J. Teuscher, T. Miyasaka, T. N. Murakami, H. J. Snaith, *Science* **2012**, *338*, 643.
[7] H.-S. Kim, C.-R. Lee, J.-H. Im, K.-B. Lee, T. Moehl, A. Marchioro, S.-J. Moon, R. Humphry-Baker, J.-H. Yum, J. E. Moser, M. Grätzel, N.-G. Park, *Sci. Rep.* **2012**, *2*, 591.
[8] L. Etgar, P. Gao, Z. S. Xue, Q. Peng, A. K. Chandiran, B. Liu, M. K. Nazeeruddin, M. Grätzel, *J. Am. Chem. Soc.* **2012**, *134*, 17396.
[9] J. H. Qiu, Y. C. Qiu, K. Y. Yan, M. Zhong, C. Mu, H. Yan, Y. H. Yang, *Nanoscale* **2013**, *5*, 3245.
[10] H.-S. Kim, J.-W. Lee, N. Yantara, P. P. Boix, S. A. Kulkarni, S. Mhaisalkar, M. Grätzel, N.-G. Park, *Nano Lett.* **2013**, *13*, 2412.
[11] E. Edri, S. Kirmayer, D. Cahen, G. Hodes, *J. Phys. Chem. Lett.* **2013**, *4*, 897.
[12] B. Cai, Y. Xing, Z. Yang, W.-H. Zhang, J. Qiu, *Energy Environ. Sci.* **2013**, *6*, 1480.
[13] J. H. Noh, S. H. Im, J. H. Heo, T. N. Mandal, S. I. Seok, *Nano Lett.* **2013**, *13*, 1764.
[14] J. M. Ball, M. M. Lee, A. Hey, H. J. Snaith, *Energy Environ. Sci.* **2013**, *6*, 1739.
[15] J. H. Heo, S. H. Im, J. H. Noh, T. N. Mandal, C.-S. Lim, J. A. Chang, Y. H. Lee, H.-J. Kim, A. Sarkar, M. K. Nazeeruddin, M. Grätzel, S. I. Seok, *Nat. Photonics* **2013**, *7*, 486.
[16] J. Burschka, N. Pellet, S.-J. Moon, R. Humphry-Baker, P. Gao, M. K. Nazeeruddin, M. Grätzel, *Nature* **2013**, *499*, 316.
[17] M. Liu, M. B. Johnston, H. J. Snaith, *Nature* **2013**, *501*, 395.
[18] D. Y. Liu, T. L. Kelly, *Nat. Photonics* **2014**, *8*, 133.
[19] O. Malinkiewicz, A. Yella, Y. H. Lee, G. M. Espallargas, M. Grätzel, M. K. Nazeeruddin, H. J. Bolink, *Nat. Photonics* **2014**, *8*, 128.
[20] Q. Chen, H. P. Zhou, Z. R. Hong, S. Luo, H.-S. Duan, H.-H. Wang, Y. S. Liu, G. Li, Y. Yang, *J. Am. Chem. Soc.* **2014**, *136*, 622.
[21] E. J. W. Crossland, N. Noel, V. Sivaram, T. Leijtens, J. A. Alexander-Webber, H. J. Snaith, *Nature* **2013**, *495*, 215.
[22] P. Docampo, J. M. Ball, M. Darwich, G. E. Eperon, H. J. Snaith, *Nat. Commun.* **2013**, *4*, 2761.
[23] H.-S. Kim, I. Mora-Sero, V. Gonzalez-Pedro, F. Fabregat-Santiago, E. J. Juarez-Perez, N.-G. Park, J. Bisquert, *Nat. Commun.* **2013**, *4*, 2242.
[24] T. Leijtens, G. E. Eperon, S. Pathak, A. Abate, M. M. Lee, H. J. Snaith, *Nat. Commun.* **2013**, *4*, 2885.
[25] W. Zhang, M. Saliba, S. D. Stranks, Y. Sun, X. Shi, U. Wiesner, H. J. Snaith, *Nano Lett.* **2013**, *13*, 4505.
[26] A. Abrusci, S. D. Stranks, P. Docampo, H.-L. Yip, A. K.-Y. Jen, H. J. Snaith, *Nano Lett.* **2013**, *13*, 3124.
[27] J. J. Choi, X. H. Yang, Z. M. Norman, S. J. L. Billinge, J. S. Owen, *Nano Lett.* **2014**, *14*, 127.
[28] G. E. Eperon, S. D. Stranks, C. Menelaou, M. B. Johnston, L. M. Herz, H. J. Snaith, *Energy Environ. Sci.* **2014**, *7*, 982.
[29] N. Pellet, P. Gao, G. Gregori, T.-Y. Yang, M. K. Nazeeruddin, J. Maier, M. Grätzel, *Angew. Chem.* **2014**, *126*, 3215; *Angew. Chem. Int. Ed.* **2014**, *53*, 3151.
[30] J. T.-W. Wang, J. M. Ball, E. M. Barea, A. Abate, J. A. Alexander-Webber, J. Huang, M. Saliba, I. Mora-Sero, J. Bisquert, H. J. Snaith, R. J. Nicholas, *Nano Lett.* **2014**, *14*, 724.
[31] A. Marchioro, J. Teuscher, D. Friedrich, M. Kunst, R. V. D. Krol, T. Moehl, M. Grätzel, J.-E. Moser, *Nat. Photonics* **2014**, *8*, 250.
[32] P.-W. Liang, C.-Y. Liao, C.-C. Chueh, F. Zuo, S. T. Williams, X.-K. Xin, J. Lin, A. K.-Y. Jen, *Adv. Mater.* **2014**, *26*, 3748.

[33] T. Baikie, Y. N. Fang, J. M. Kadro, M. Schreyer, F. X. Wei, S. G. Mhaisalkar, M. Grätzel, T. J. White, *J. Mater. Chem. A* **2013**, *1*, 5628.
[34] H. J. Snaith, R. Humphry-Baker, P. Chen, I. Cesar, S. M. Zakeeruddin, M. Grätzel, *Nanotechnology* **2008**, *19*, 424003.
[35] I. K. Ding, N. Tétreault, J. Brillet, B. E. Hardin, E. H. Smith, S. J. Rosenthal, F. Sauvage, M. Grätzel, M. D. Mcgehee, *Adv. Funct. Mater.* **2009**, *19*, 2431.
[36] G. E. Eperon, V. M. Burlakov, P. Docampo, A. Goriely, H. J. Snaith, *Adv. Funct. Mater.* **2014**, *24*, 151.
[37] A. Dualeh, T. Moehl, N. Tétreault, J. Teuscher, P. Gao, M. K. Nazeeruddin, M. Grätzel, *ACS Nano* **2014**, *8*, 362.
[38] H. J. Snaith, A. Abate, J. M. Ball, G. E. Eperon, T. Leijtens, N. K. Noel, S. D. Stranks, J. T.-W. Wang, K. Wojciechowski, W. Zhang, *J. Phys. Chem. Lett.* **2014**, *5*, 1511.
[39] H. A. Atwater, A. Polman, *Nat. Mater.* **2010**, *9*, 205.
[40] M. Law, L. E. Greene, J. C. Johnson, R. Saykally, P. D. Yang, *Nat. Mater.* **2005**, *4*, 455.
[41] J. B. You, L. T. Dou, K. Yoshimura, T. Kato, K. Ohya, T. Moriarty, K. Emery, C.-C. Chen, J. Gao, G. Li, Y. Yang, *Nat. Commun.* **2013**, *4*, 1446.

